Electronic Supplementary Material (ESI) for Chemical Science

Electronic supplementary information

Modifying the properties of 4f single-ion magnets by peripheral ligand functionalisation

Kasper S. Pedersen, Liviu Ungur, Marc Sigrist, Alexander Sundt, Magnus Schau-Magnussen, Veacheslav Vieru, Hannu Mutka, Stephane Rols, Høgni Weihe, Oliver Waldmann, Liviu F. Chibotaru, Jesper Bendix, and Jan Dreiser

Table of content

1 Crystallography

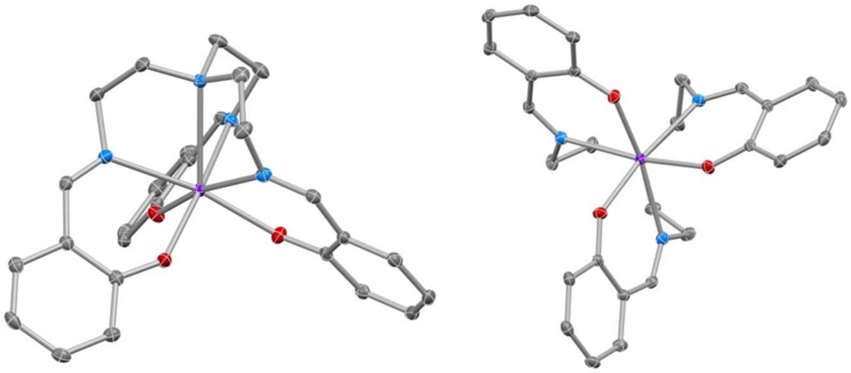

Fig. S1. Structure of **1** at *T* = 122 K shown in perspective (left) and along the three-fold rotation axis (right) The ellipsoids are drawn at 50 % probability level. Hydrogen atoms are omitted for clarity.

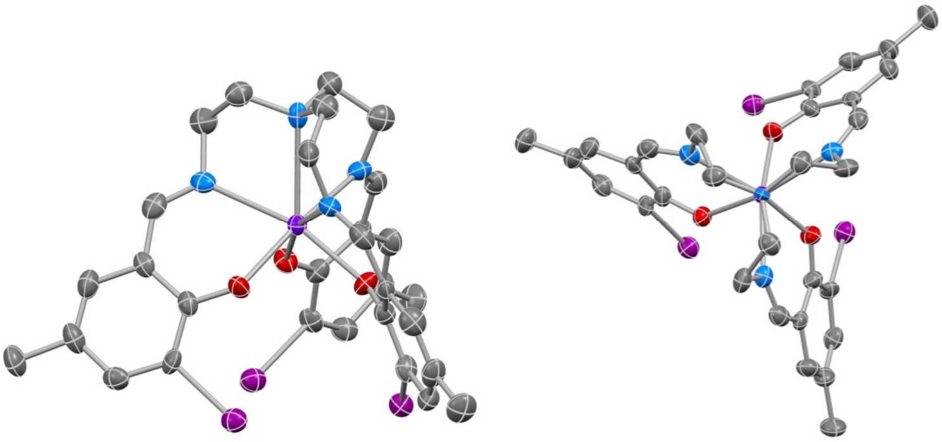

Fig. S2. Structure of **2** at *T* = 122 K shown in perspective (left) and along the three-fold rotation axis (right). The ellipsoids are drawn at 50 % probability level. Hydrogen atoms are omitted for clarity. With an Er-I distance of 4.996Å the Er centre must be considered 7-coordinated.

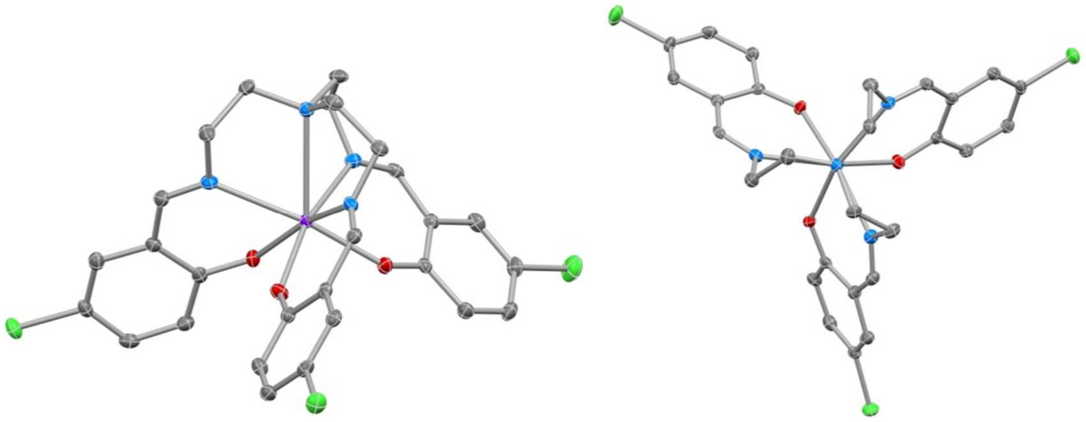

Fig. S3. Structure of **recrystallised 3** at *T* = 122 K. The ellipsoids are drawn at 50 % probability level. Hydrogen atoms are omitted for clarity.

Table S1. Crystallographic data and refinement parameters for **1**–**3**.

	1	**2**	**Recrystallised 3**
formula	$C_{27}H_{27}ErN_4O_3$	$C_{30}H_{30}ErI_3N_4O_3$	$C_{27}H_{24}Cl_3ErN_4O_3$
M_r/g mol^{-1}	622.80	1042.57	726.11
color, shape	Pale pink, pencil	Yellow, pencil	Yellow, block
crystal size/mm	0.13 × 0.13 × 0.11	N/A	0.19 × 0.16 × 0.07
crystal system	Trigonal	Trigonal	Monoclinic
space group	$P\bar{3}c1$	$P\bar{3}$	$P2_1/c$
T/K	122(1)	122(1)	122(1)
a/Å	12.9479(5)	13.0245	12.5689(4)
b/Å	12.9479(5)	13.0245	15.0967(5)
c/Å	16.3112(5)	11.15(8)	14.9942(5)
V/Å^3	2368.18(15)	1638(12)	2673.89(15)
α/°	90	90	90
β/°	90	90	109.980(1)
γ/°	120	120	90
Z	4	2	4
ρ_{calc}/g cm^{-3}	1.747	2.113	1.804
F_{000}	1236	975.0	1428
μ(Mo K_α)/mm^{-1}	3.58	5.42	3.48
θ range/°	2.5–30.5	1.8–27.5	3.1–25.5
collected reflns	9895	60430	84177
unique reflns	2425	2519	5071
params/restraints	105/0	123/0	343/0
reflns ($I > 2\sigma(I)$)	1799	1881	4354
GoF	1.02	1.10	1.10
$R_1{}^a$($I > 2.00\sigma(I)$)	0.020	0.065	0.020
$wR_2{}^b$(all data)	0.047	0.176	0.046
max/min $\Delta\rho_{□}$□e Å^{-3}	0.96/−0.72	2.36/−1.94	0.59/−0.31

$R_1 = \Sigma||F_o| - |F_c||/\Sigma|F_o|$. $^b wR_2 = [\Sigma w(F_o{}^2 - F_c{}^2)^2/\Sigma w(F_o{}^2)^2]^{1/2}$

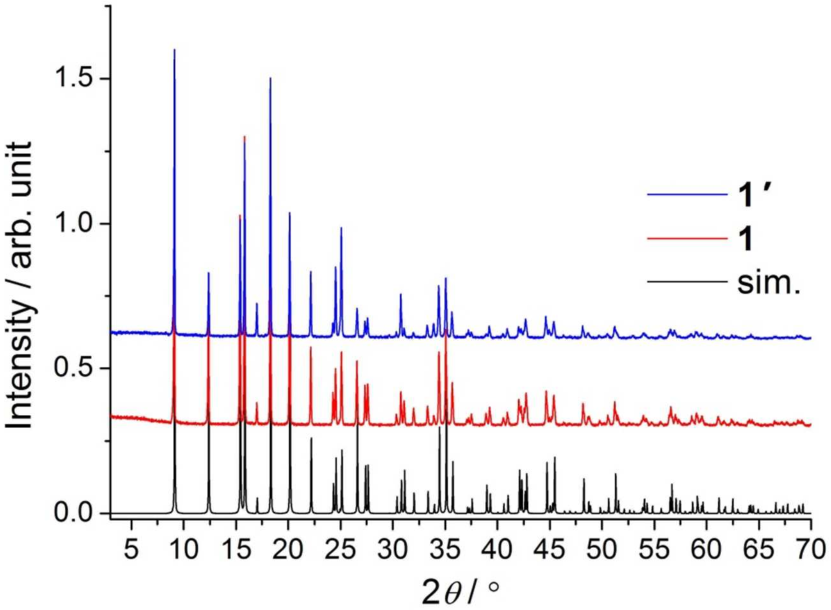

Fig. S4. Experimental (room temperature) and calculated X-ray powder diffractograms of **1** and **1′**.

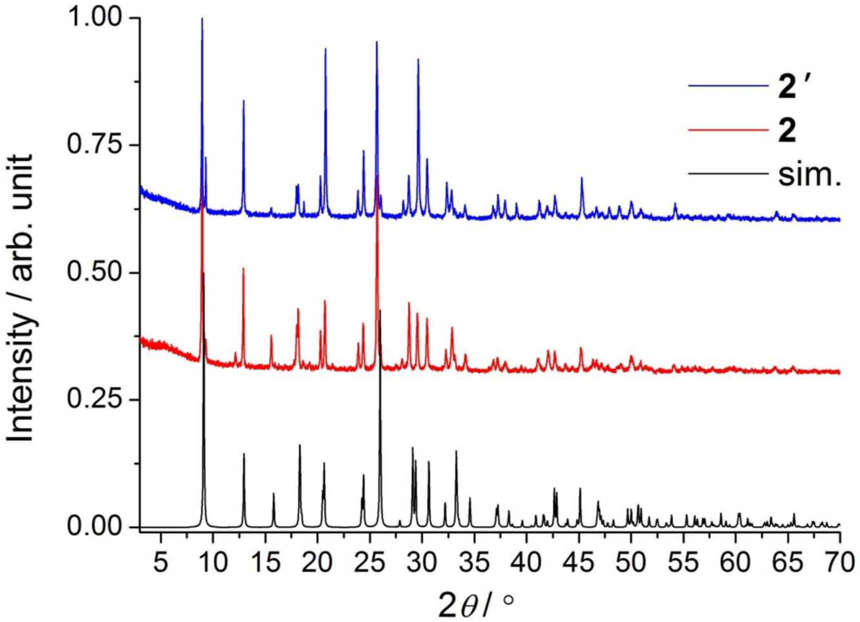

Fig. S5. Experimental (room temperature) and calculated X-ray powder diffractograms of **2** and **2′**.

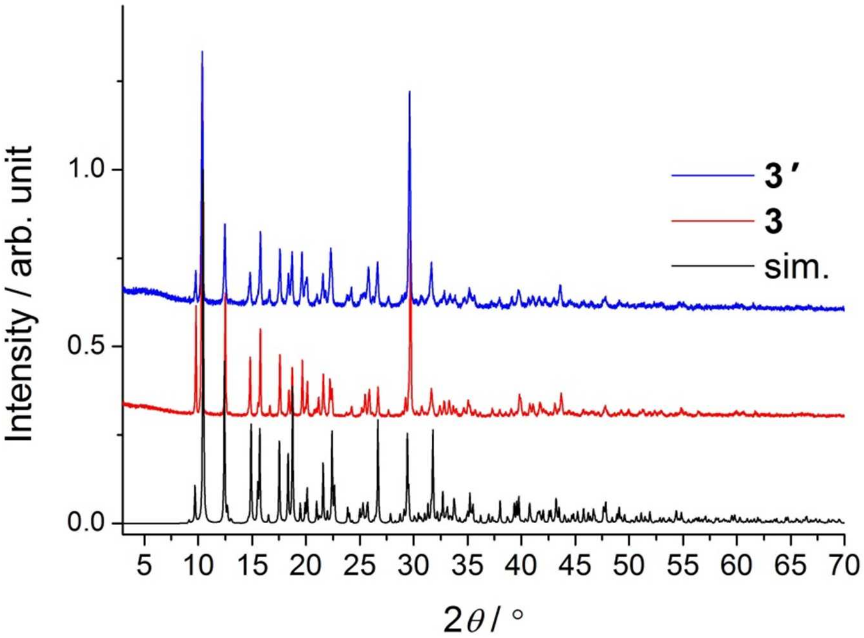

Fig. S6. Experimental (room temperature) and calculated X-ray powder diffractograms of **3** and **3′**.

2 Inelastic neutron scattering

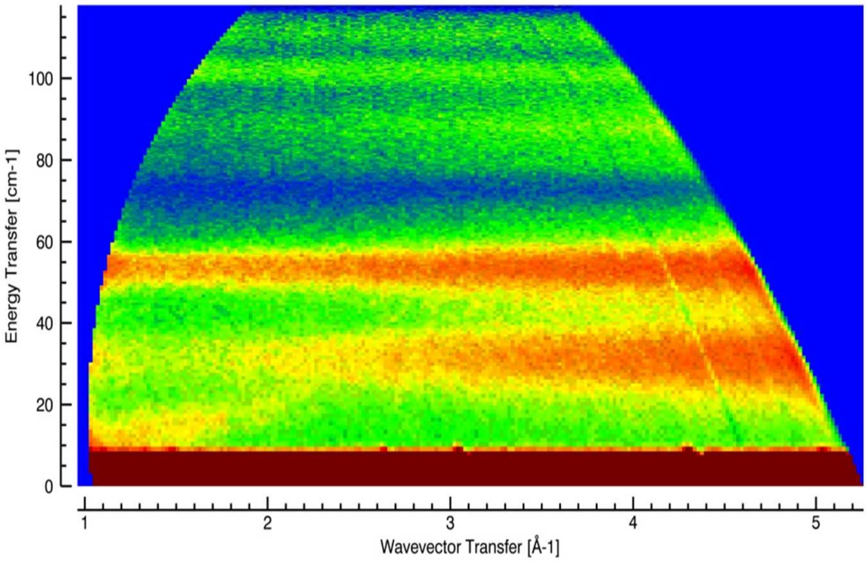

Fig. S7. $S(|\mathbf{Q}|,E)$ map for **1** obtained with λ_i = 2.2 Å at 1.5 K.

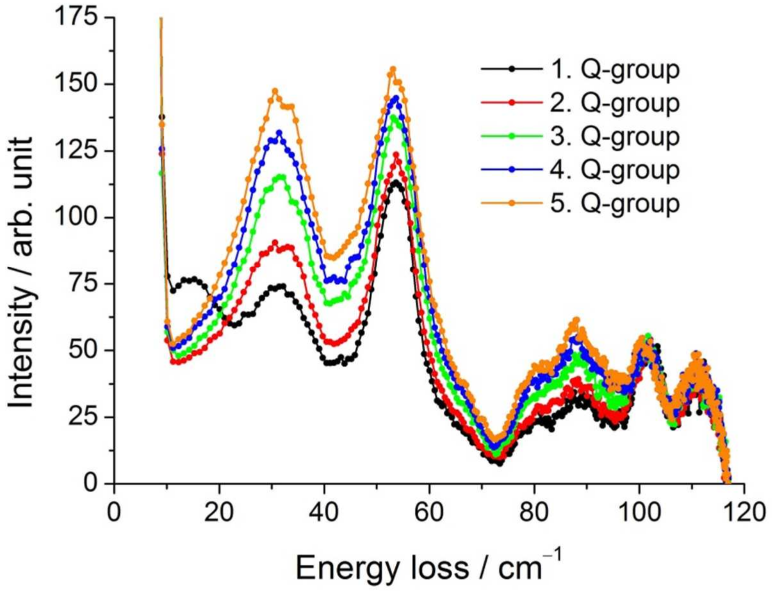

Fig. S8. Integrated INS spectra of **1** λ_i = 2.2 Å at 1.5 K summed over all detector divided into 5 groups. "1. Q-group" corresponds to the smallest scattering angles and "5. Q-group" to the highest scattering angles.

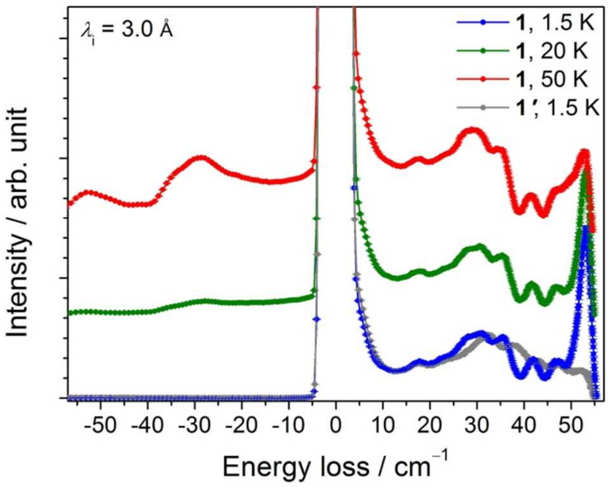

Fig. S9. INS spectra of **1** obtained with λ_i = 3.0 Å at 1.5 K, 20 K and 50 K. The 1.5 K spectrum of **1′** is shown for comparison. The spectra are offset to improve clarity.

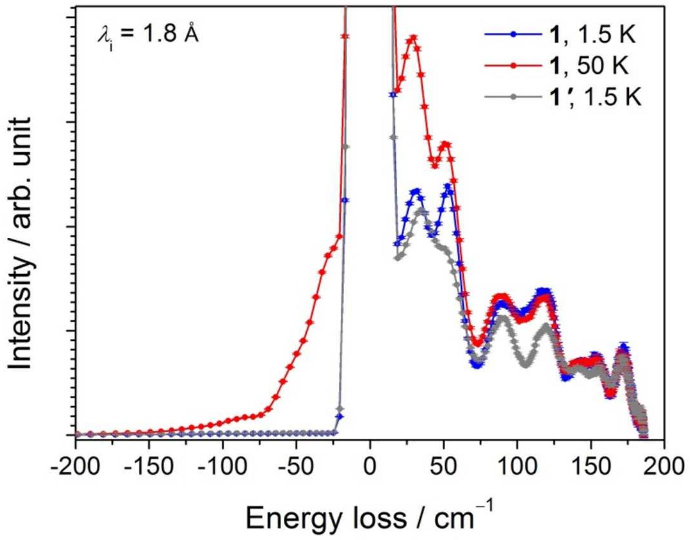

Fig. S10. INS spectra of **1** obtained with λ_i = 1.8 Å at 1.5 K and 50 K. The 1.5 K spectrum of **1′** is shown for comparison.

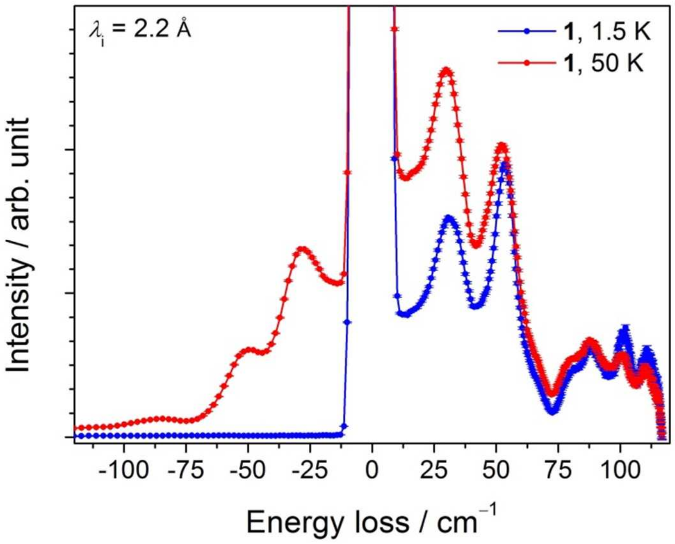

Fig. S11. INS spectra of **1** obtained with λ_i = 2.2 Å at 1.5 K and 50 K.

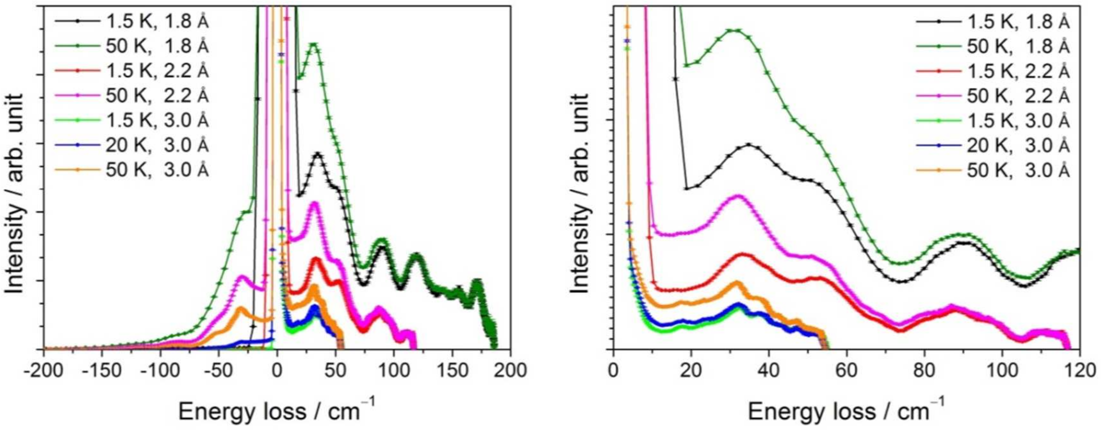

Fig. S12. Temperature and incident wavelength dependence of the INS spectra of **1′**. The spectrum to the right is a zoom of the 0–120 cm^{-1} energy loss window.

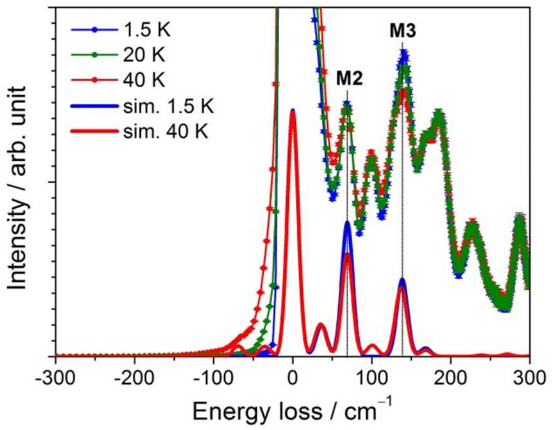

Fig. S13. Temperature dependence of INS spectra of **2** obtained with λ_i = 1.4 Å at the indicated temperatures. The thick, solid lines are simulations using the parameters given in the main text.

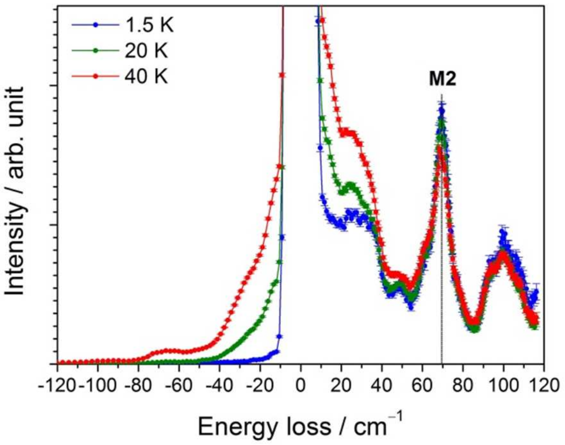

Fig. S14. Temperature dependence of INS spectra of **2** obtained with λ_i = 2.2 Å at the indicated temperatures.

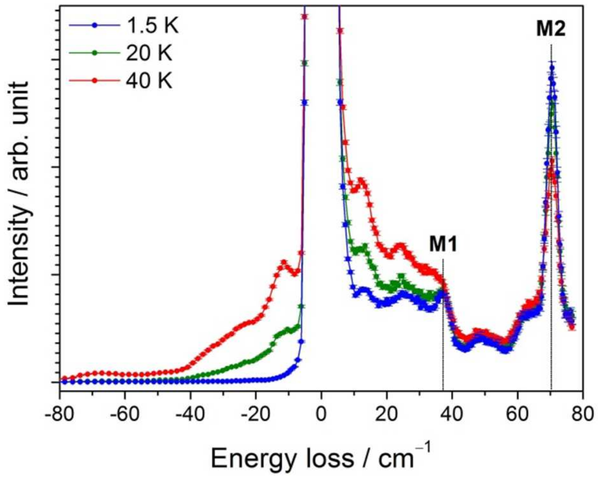

Fig. S15. Temperature dependence of INS spectra of **2** obtained with λ_i = 2.8 Å at the indicated temperatures.

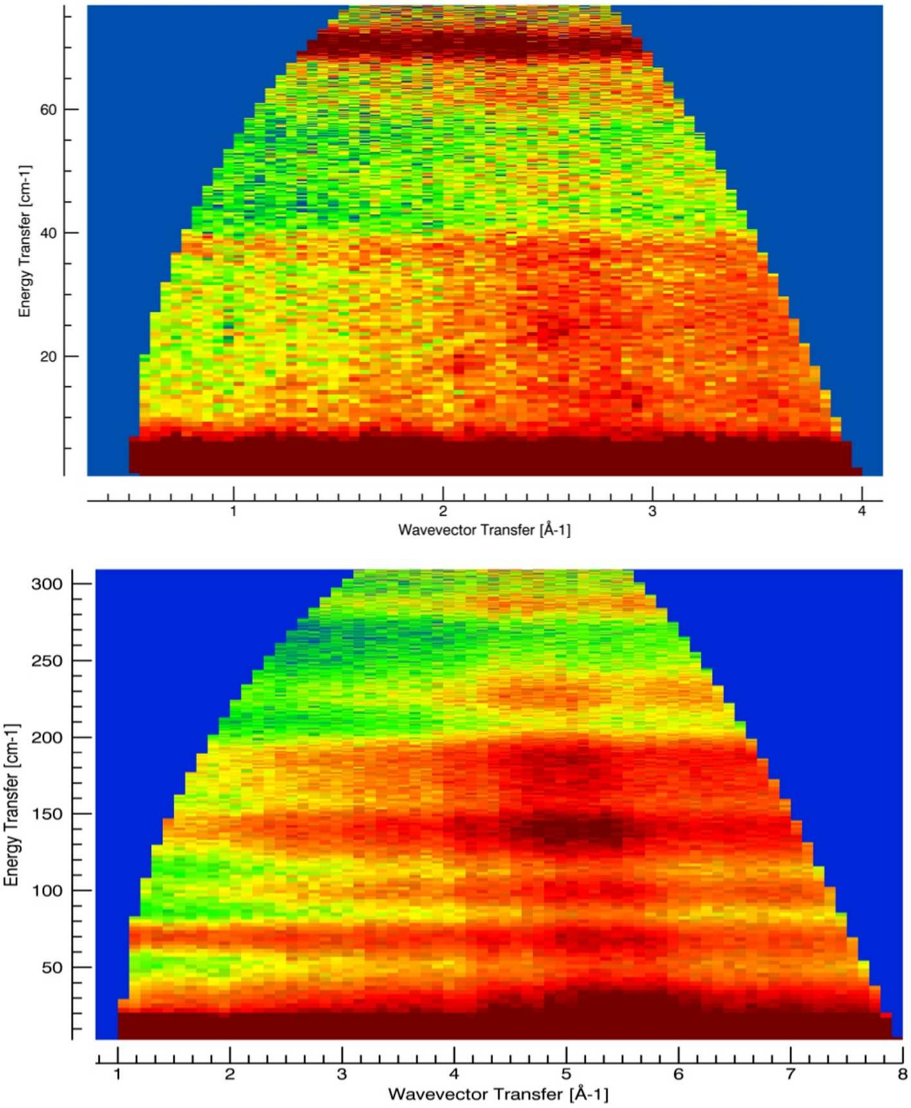

Fig. S16. $S(|\mathbf{Q}|,E)$ for **2** obtained with λ_i = 2.8 Å (upper panel) and 1.4 Å (lower panel) at 1.5 K.

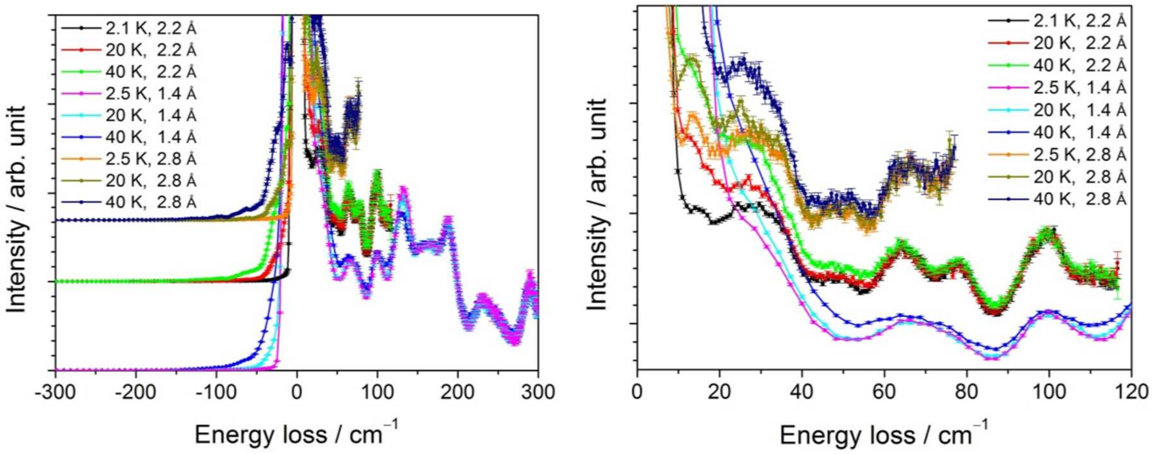

Fig. S17. Temperature and incident wavelength dependence of the INS spectra of **2′** measured on IN4. The spectrum to the right is a zoom of the 0–120 cm^{-1} energy loss window.

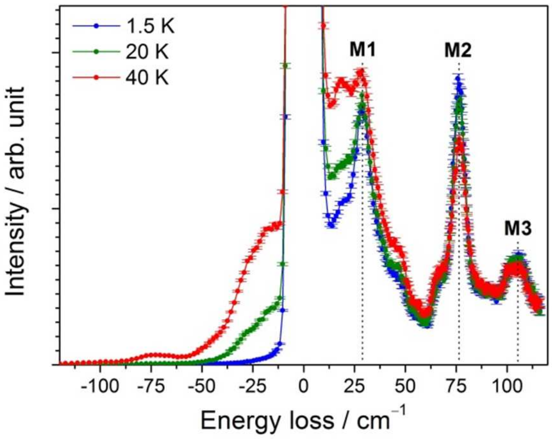

Fig. S18. Temperature dependence of INS spectra of **3** obtained with λ_i = 2.2 Å at the indicated temperatures.

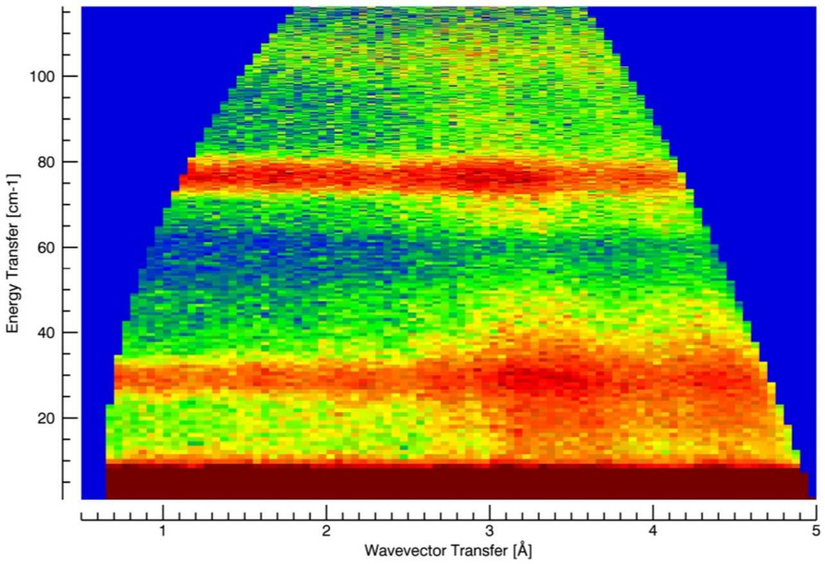

Fig. S19. $S(|\mathbf{Q}|,E)$ map for **3** obtained with λ_i = 2.2 Å at 1.5 K.

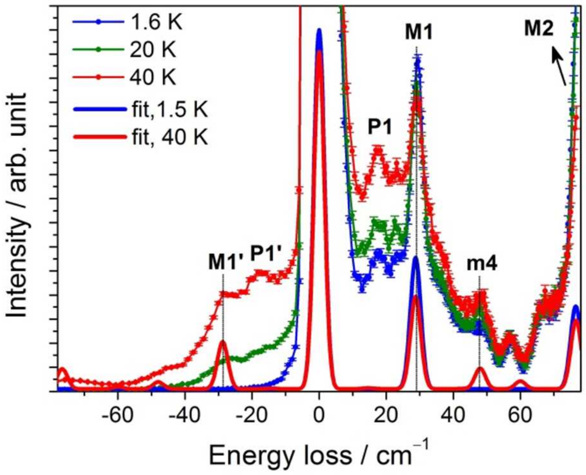

Fig. S20. Temperature dependence of INS spectra of **3** obtained with λ_i = 2.8 Å at the indicated temperatures. The thick, solid lines are simulations using the parameters given in the main text.

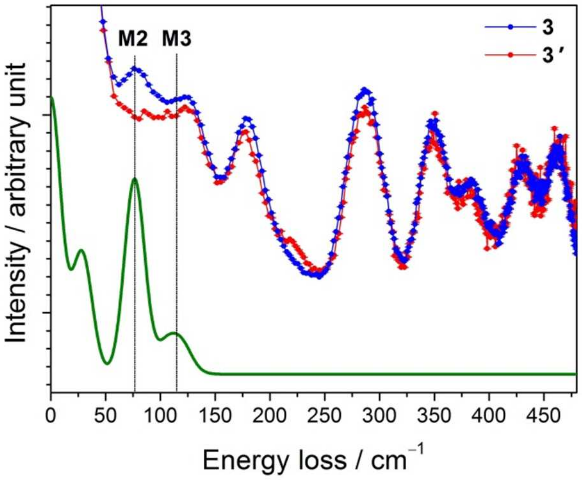

Fig. S21. Temperature dependence of INS spectra of **3** and **3′** obtained with λ_i = 1.1 Å at T = 1.5 K. The green, solid line is a simulation of the magnetic transitions in **3** using the parameters given in the main text.

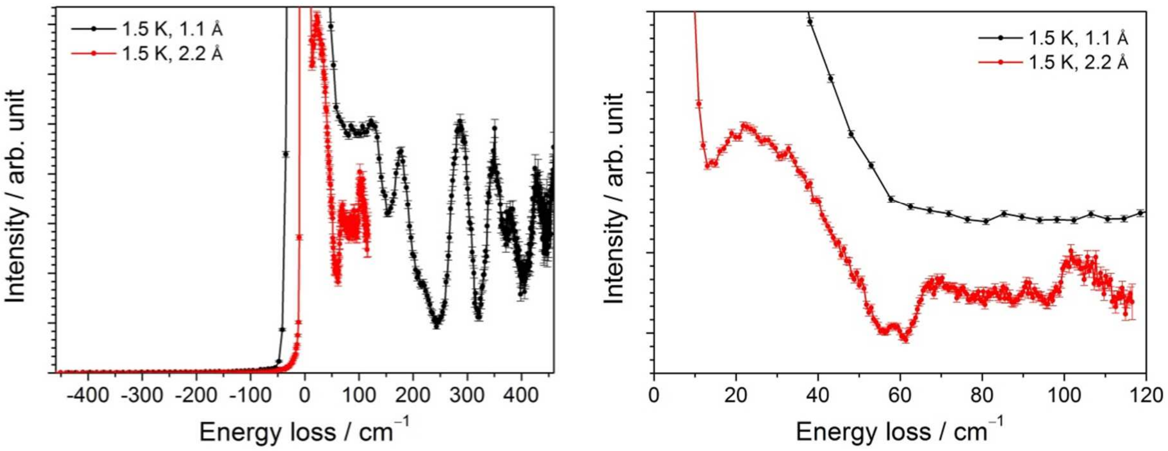

Fig. S22. Temperature and incident wavelength dependence of the INS spectra of **3′** measured on IN4. The spectrum to the right is a zoom of the 0–120 cm^{-1} energy loss window.

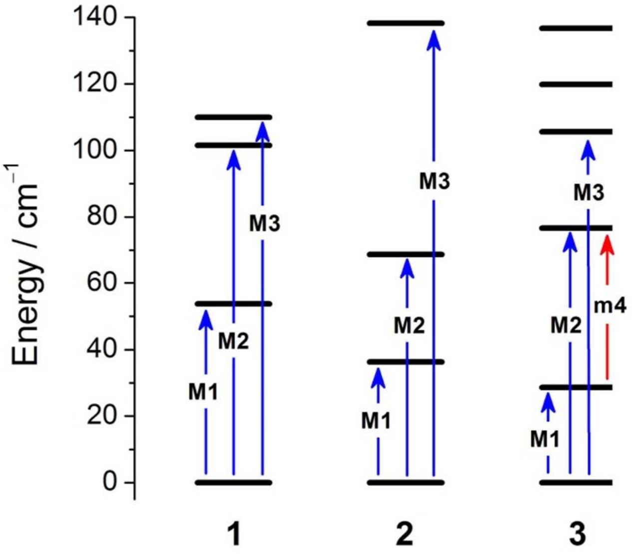

Fig. S23. Overview of the low-energy transitions observed by INS for **1**–**3**. The energy level diagrams were calculated from the best-fit parameters as described in the main text.

3 Dc magnetic data

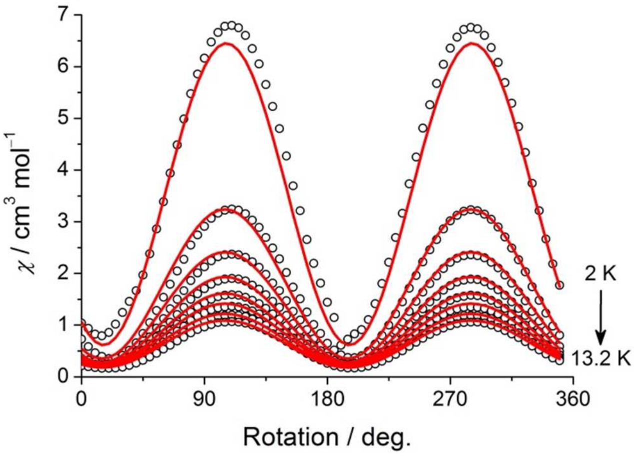

Fig. S24. Angular dependence of the magnetic susceptibility (H_{dc} = 2000 Oe) for a single crystal of **1**. The solid red lines are calculated from the best fit parameters and the angular dependence of the form $\chi(\theta) = \chi_{parallel}\sin^2(\theta-\varphi) + \chi_{perpendicular}\cos^2(\theta-\varphi)$ where θ is the angle and φ is a constant phase shift.

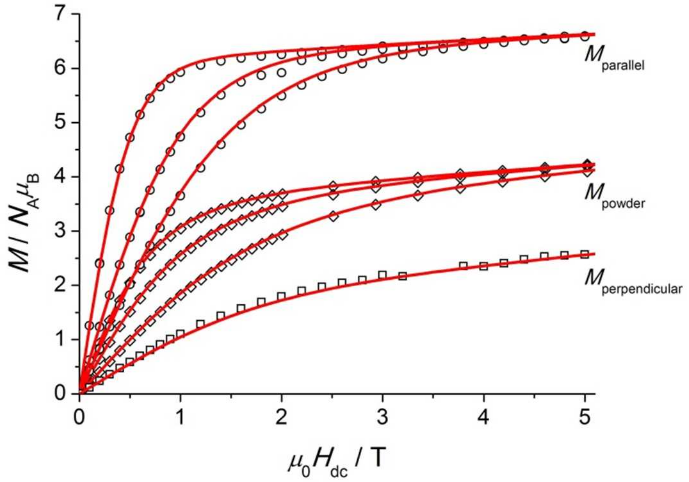

Fig. S25. Temperature dependence of the magnetization for **1**. Parallel (2, 4, 6 K); powder (2, 3, 5 K). The solid lines are the best fit using the parameters given in the main text.

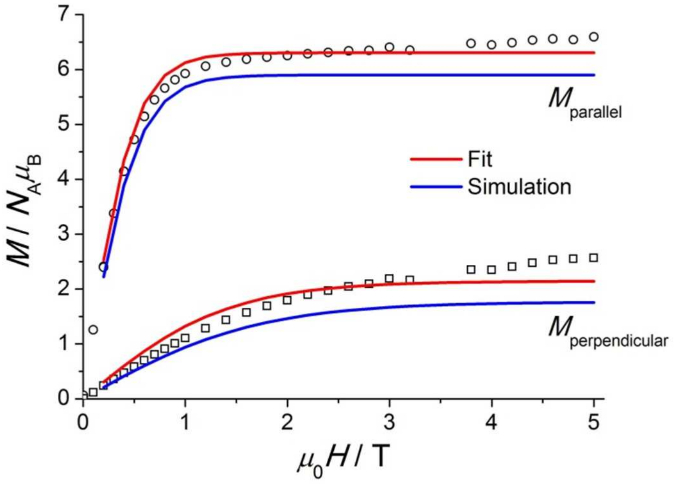

Fig. S26. Simulation and fit of the parallel and perpendicular magnetization of **1** at $T = 2$ K when treated as an effective $S = ½$ with an anisotropic g-factor. The best-fit result (red line) is calculated from $g_{parallel} = 12.6(7)$ and $g_{perpendicular} = 4.3(7)$.

4 EPR spectroscopy

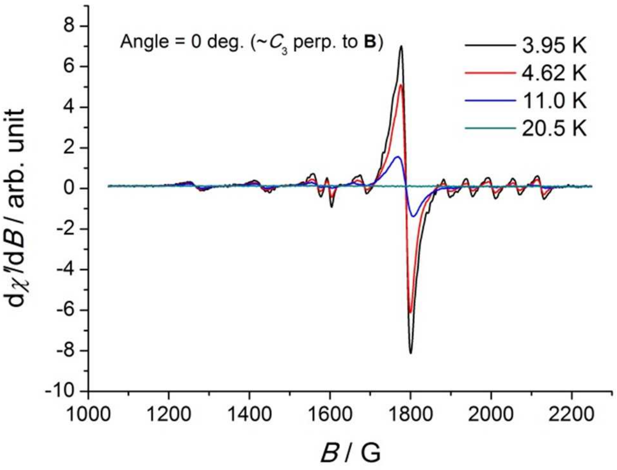

Fig. S27. Temperature dependence of the EPR resonances in Er:**1′**(~5% doping) when the field is applied perpendicular to the C_3 axis.

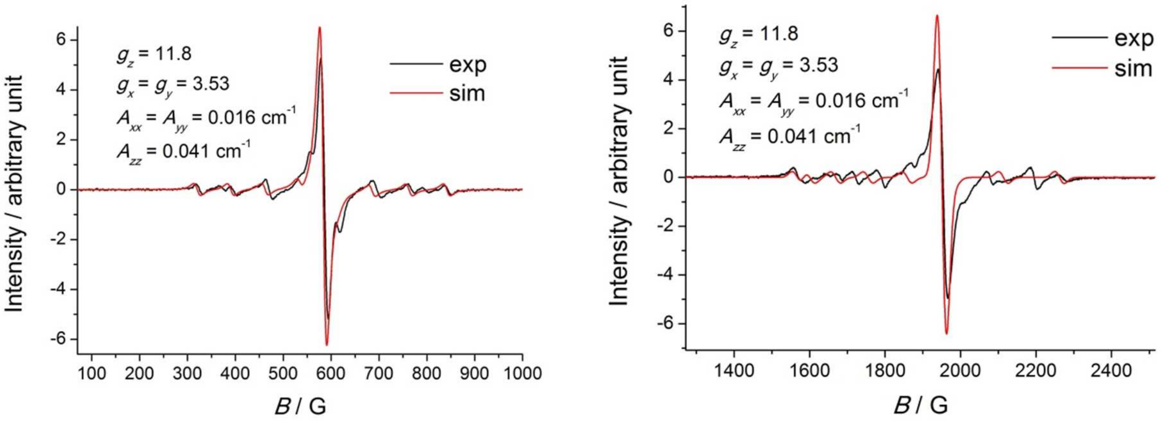

Fig. S28. X-band EPR spectra of Er:**1′** (~5% doping) and simulations of the field orientations along (left) and perpendicular (right) to the C_3 axis.

5 CASSCF calculations

Table S2. Contractions of the employed basis sets for all atoms.

Atom	Employed basis set
Er	8s7p5d3f2g1h
I	6s5p2d
Cl	4s3p
N	4s3p2d1f
O	4s3p2d1f
C	3s2p1d
C	3s2p
H	2s

Table S3. Ab initio calculated energies of the low-lying Kramers doublets in complex **1,** using the experimental structure determined at 122K.

Multiplet	One molecule	One molecule embedded in 5 layers of point charges	Observed
$^4I_{15/2}$	0 67 100 104 199 428 465 491	0 58 95 95 201 419 457 481	0 54 102 110 299 568 610 642
$^4I_{13/2}$	6653 6689 6694 6706 6909 6909 6923	6651 6682 6688 6704 6900 6900 6913	6594 6612 6621 6690 6909 6928 6939
$^4I_{11/2}$	10718 10725 10741 10868 10874 10888	10713 10724 10735 10860 10866 10879	10291 10301 10316 10444 10449 10510

Table S4. Comparison of *ab initio* calculated Extended Stevens parameters describing the splitting of the ground ionic multiplet J=15/2 for complex **1** using the experimental structure determined at 122 K (two left columns) and at 283 K (third and fourth columns).

k,q	One molecule (122K)	One molecule embedded in 5	One molecule (283K)	One molecule embedded in 5	ratio between CF parameters	ratio between CF parameters

		layers of point charges (122K)		layers of point charges (283K)	122K/283K, one molecule	122K/283K, one molecule embedded in 5 layers of point charges
2,-2	0.1232673E-02	0.1139505E-02	$-0.3681437 \times 10^{-2}$	$-0.3531750 \times 10^{-2}$	0.32755	0.30854
2,-1	-0.5877685E-02	-0.4715030E-02	$-0.1219041 \times 10^{-1}$	$-0.1114168 \times 10^{-1}$	1.16077	1.06259
2,0	-0.1050594E+01	-0.9599914E+00	-0.9979328	-0.8775679	1.05277	1.09392
2,1	0.9808823E-02	0.7767015E-02	$-0.8113687 \times 10^{-2}$	$-0.7135038 \times 10^{-2}$	1.18771	1.32815
2,2	-0.8658971E-03	-0.7657797E-03	0.7419442×10^{-3}	0.1056477×10^{-2}	1.10928	0.87559
4,-4	-0.1501604E-03	-0.1269086E-03	0.5873959×10^{-4}	0.2149742×10^{-4}	-4.15181	-3.71540
4,-3	0.7976303E-01	0.7898635E-01	0.1599697	0.1529677	0.95540	0.95736
4,-2	0.2111123E-04	0.1958624E-04	$-0.2383821 \times 10^{-3}$	$-0.2386823 \times 10^{-3}$	0.12364	0.13227
4,-1	-0.3381748E-04	-0.3330333E-04	$-0.8694542 \times 10^{-4}$	$-0.9511601 \times 10^{-4}$	0.51869	0.52356
4,0	-0.9263096E-03	-0.9080429E-03	$-0.1058415 \times 10^{-2}$	$-0.1010250 \times 10^{-2}$	0.87515	0.89877
4,1	0.9371012E-04	0.9213955E-04	$-0.7570600 \times 10^{-4}$	$-0.7225837 \times 10^{-4}$	1.26322	1.23173
4,2	-0.1709902E-03	-0.1452943E-03	$-0.9256999 \times 10^{-4}$	$-0.9229038 \times 10^{-4}$	-3.25135	-3.51021
4,3	-0.1594099E+00	-0.1592970E+00	$-0.7776269 \times 10^{-1}$	$-0.8906691 \times 10^{-1}$	-1.01497	-1.01719
4,4	0.1323111E-03	0.1162745E-03	$-0.2590784 \times 10^{-3}$	$-0.2654719 \times 10^{-3}$	-0.69580	-0.69946
6,-6	-0.7091608E-03	-0.7216960E-03	$-0.6744938 \times 10^{-3}$	$-0.7609830 \times 10^{-3}$	-0.99652	-0.99783
6,-5	-0.6910605E-05	-0.6399478E-05	0.2691267×10^{-5}	0.5177126×10^{-5}	-0.42261	-0.42721
6,-4	0.1243406E-05	0.9850875E-06	$-0.9849005 \times 10^{-7}$	0.4580021×10^{-6}	21.03379	6.94843
6,-3	-0.4823925E-03	-0.5216402E-03	$-0.7482363 \times 10^{-3}$	$-0.6968011 \times 10^{-3}$	1.01920	1.02182
6,-2	-0.3212288E-06	-0.3716844E-06	0.4125936×10^{-5}	0.4289042×10^{-5}	0.10328	0.13091
6,-1	0.2534802E-05	0.1898686E-05	0.7273274×10^{-5}	0.7593575×10^{-5}	0.80259	0.73527
6,0	0.9769772E-04	0.9652236E-04	0.9780098×10^{-4}	0.9684224×10^{-4}	0.99891	0.99666
6,1	-0.4995730E-05	-0.3885737E-05	0.5266792×10^{-5}	0.4718506×10^{-5}	1.10488	1.13254
6,2	0.2923507E-05	0.2534176E-05	0.1784945×10^{-5}	0.1586536×10^{-5}	-2.27947	-2.42621
6,3	0.7668886E-03	0.7537401E-03	0.4465089×10^{-3}	0.5404041×10^{-3}	-1.04817	-1.04819
6,4	-0.6138114E-06	-0.3575995E-06	0.2315290×10^{-5}	0.2359842×10^{-5}	-0.49100	-0.38915
6,5	0.9343445E-05	0.7894580E-05	0.2085818×10^{-4}	0.2052274×10^{-4}	-2.44521	-1.90042
6,6	0.5320969E-03	0.5228729E-03	$-0.5382682 \times 10^{-3}$	$-0.4142453 \times 10^{-3}$	1.09009	1.09601

Table S5. Ab initio calculated *g* tensors of the low-lying Kramers doublets in complex **1.**

KD	g	structure determined at room temperature		structure determined at 122K	
		One molecule	One molecule embedded in 5 layers of point charges	One molecule	One molecule embedded in 5 layers of point charges
1	g_X	1.8257	2.2779	1.8503	2.1844
	g_Y	1.8280	2.2815	1.8505	2.1847
	g_Z	14.2567	13.6758	14.2357	13.8050
2	g_X	7.8218	7.6465	7.5926	7.5380
	g_Y	7.7637	7.5900	7.5898	7.5363
	g_Z	2.2389	2.8702	2.1984	2.7184
3	g_X	0.0076	0.1650	0.2509	0.0054
	g_Y	0.1898	0.3090	0.2654	0.3561
	g_Z	10.9449	5.9540	10.8943	10.9341
4	g_X	0.0568	0.0419	0.0046	0.1479
	g_Y	0.0742	0.5095	0.0087	0.1763
	g_Z	6.0397	10.9413	6.2302	6.1242
5	g_X	0.0016	0.0016	0.0000	0.0000
	g_Y	0.0021	0.0021	0.0004	0.0005
	g_Z	17.2416	17.3505	17.0952	17.1846
6	g_X	7.2124	7.1979	7.2281	7.2230
	g_Y	7.1435	7.1290	7.2255	7.2209
	g_Z	3.2719	3.3182	3.1830	3.2106
7	g_X	0.0085	0.0066	0.0006	0.0007
	g_Y	0.0723	0.0754	0.0053	0.0049

	g_Z	7.3194	7.3696	7.2235	7.2603
8	g_X	7.3622	7.3769	7.3654	7.3816
	g_Y	7.2891	7.2982	7.3576	7.3741
	g_Z	3.7298	3.7197	3.6527	3.6321

Table S6. Ab initio calculated energies of the low-lying Kramers doublets in complex **2,** using the experimental structure determined at 120 K.

Multiplet	One molecule	One molecule embedded in 5 layers of point charges
$^4I_{15/2}$	0.0	0.0
	13.2	13.5
	54.3	52.8
	69.1	68.4
	202.6	201.2
	333.2	331.8
	376.8	375.6
	397.0	395.4
$^4I_{13/2}$	6626.1	6625.3
	6640.9	6640.0
	6642.1	6641.6
	6704.9	6704.2
	6830.9	6829.8
	6831.3	6830.1
	6844.6	6843.4
$^4I_{11/2}$	10680.8	10679.9
	10682.6	10682.0
	10718.0	10717.3
	10801.5	10800.5
	10802.9	10801.8
	10812.0	10810.9

Table S7. Comparison of *ab initio* calculated Extended Stevens parameters describing the splitting of the ground ionic multiplet J=15/2 for complex **2** using the experimental structure determined at 120 K.

k,q	One molecule	One molecule embedded in 5 layers of point charges	ratio between CF parameters of one molecule alone and one molecule embedded in 5 layers of point charges
2,-2	0.87741876816112E-03	0.20762471839075E-02	0.42260
2,-1	0.77110694747482E-02	0.68239195893284E-02	1.13001
2,0	-0.28835114103462E+00	-0.28244479695370E+00	1.02091
2,1	0.39195860493380E-03	-0.15661726355710E-02	-0.25027
2,2	0.37272467019423E-02	0.30596955156197E-02	1.21818
4,-4	-0.14638066056466E-03	-0.12557270644692E-03	1.16570
4,-3	-0.11130962450366E+00	-0.11134026964821E+00	0.99972
4,-2	-0.17134190041980E-03	-0.15132409898807E-03	1.13228
4,-1	0.14302278271712E-03	0.13699741474353E-03	1.04398
4,0	-0.14784196634766E-02	-0.14607934277829E-02	1.01207
4,1	0.11633507503265E-04	0.11466711657926E-04	1.01455
4,2	-0.12953643613042E-03	-0.12004181533053E-03	1.07909
4,3	0.12960589792367E+00	0.12933748921357E+00	1.00208
4,4	-0.16370267499154E-03	-0.15163913406654E-03	1.07955
6,-6	-0.71488020665151E-03	-0.71718706994000E-03	0.99678
6,-5	-0.66059410175749E-05	-0.61361522720372E-05	1.07656
6,-4	0.11172100738822E-05	0.10138058729890E-05	1.10200

6,-3	0.18265208250289E-03	0.16028434479981E-03	1.13955
6,-2	0.23783104155847E-05	0.21607829979088E-05	1.10067
6,-1	-0.75086715025129E-05	-0.63839082636963E-05	1.17619
6,0	0.90273646940464E-04	0.88958353624638E-04	1.01479
6,1	0.30852990462234E-07	-0.13273482538697E-07	-2.32441
6,2	0.23054258178202E-07	-0.15354511954771E-06	-0.15015
6,3	-0.52590240099472E-03	-0.54494962238283E-03	0.96505
6,4	0.10722377784107E-06	-0.53844996530477E-07	-1.99134
6,5	-0.39481785285863E-05	-0.24875223014113E-05	1.58719
6,6	0.13956195697666E-03	0.15068938405227E-03	0.92616

Table S8. Ab initio calculated *g* tensors of the low-lying Kramers doublets in complex **2.**

KD	g	One molecule	One molecule embedded in 5 layers of point charges
1	g_X	4.9617	5.2684
	g_Y	4.9681	5.2827
	g_Z	8.6599	7.7902
2	g_X	5.0567	4.2912
	g_Y	5.1035	4.3422
	g_Z	7.1836	7.9687
3	g_X	0.0144	0.0105
	g_Y	0.0563	0.0629
	g_Z	5.0631	5.0913
4	g_X	1.2738	1.3903
	g_Y	1.3293	1.4441
	g_Z	9.9846	9.8845
5	g_X	0.0014	0.0020
	g_Y	0.0022	0.0026
	g_Z	17.4077	17.3526
6	g_X	7.1280	7.1530
	g_Y	7.0525	7.0816
	g_Z	3.6493	3.6043
7	g_X	0.0199	0.0142
	g_Y	0.1146	0.1047
	g_Z	8.3145	8.3175
8	g_X	7.5370	7.5616
	g_Y	7.3836	7.4249
	g_Z	3.7968	3.7360

Table S9. Ab initio calculated energies of the low-lying Kramers doublets in complex **3** using the experimental structure determined at room temperature.

Multiplet	One molecule	One molecule embedded in 5 layers of point charges
$^4I_{15/2}$	0.0	0.0
	21.3	15.8
	64.1	59.8
	73.7	70.4
	172.0	173.4
	288.6	285.8
	325.2	323.6
	347.0	340.1

Table S10. Ab initio calculated *g* tensors of the low-lying Kramers doublets in complex **3.**

KD	g	One molecule	One molecule embedded in 5 layers of point charges
1	g_X	0.8675	0.5256
	g_Y	1.3002	1.6185
	g_Z	14.1015	13.0732
2	g_X	1.6844	2.2014
	g_Y	5.8146	5.0943
	g_Z	11.4051	11.0154
3	g_X	6.8371	1.7764
	g_Y	6.0712	4.2489
	g_Z	0.7042	7.0202
4	g_X	3.6341	3.5277
	g_Y	6.0558	5.9146
	g_Z	9.4633	9.3925
5	g_X	0.0479	0.0341
	g_Y	0.0628	0.0466
	g_Z	17.5022	17.4549
6	g_X	1.9039	2.5227
	g_Y	4.0511	3.4602
	g_Z	10.9662	10.9757
7	g_X	9.2524	7.4312
	g_Y	5.7468	5.2721
	g_Z	1.2163	2.9296
8	g_X	2.0464	2.4351
	g_Y	2.6725	5.9222
	g_Z	13.2531	9.6348

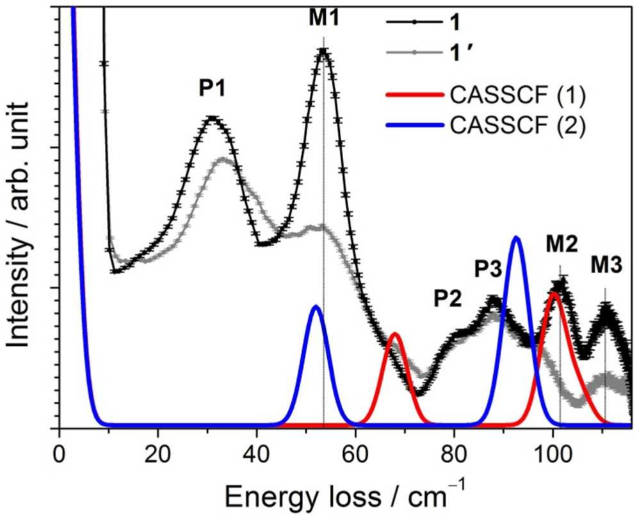

Fig. S29. Experimental and calculated INS spectrum of **1** using the CASSCF derived parameters. CASSCF (1) and (2) refer to the calculations for an isolated molecule and taking into account additional point charges, respectively.

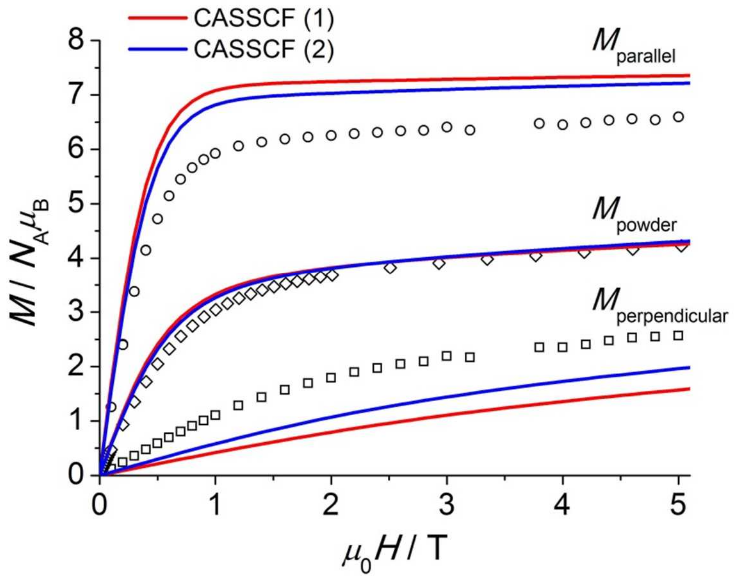

Fig. S30. Experimental (powdered sample and parallel and perpendicular to the C_3 axis for a single crystal) and calculated magnetization curves for **1** using the CASSCF derived parameters. CASSCF (1) and (2) refer to the calculations for an isolated molecule and taking into account additional point charges, respectively.

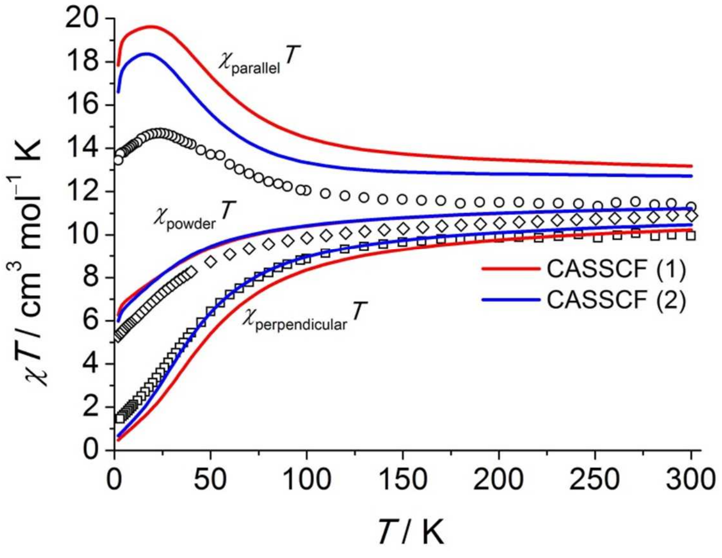

Fig. S31. Experimental (powdered sample and parallel and perpendicular to the C_3 axis for a single crystal) and calculated χT curves for **1** using the CASSCF derived parameters. CASSCF (1) and (2) refer to the calculations for an isolated molecule and taking into account additional point charges, respectively.

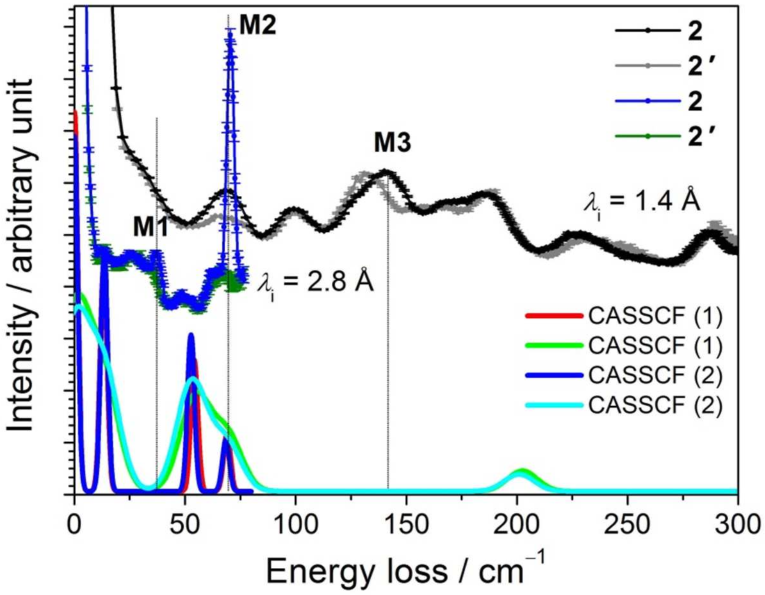

Fig. S32. Experimental and calculated INS spectrum of **2** using the CASSCF derived parameters. CASSCF (1) and (2) refer to the calculations for an isolated molecule and taking into account additional point charges, respectively.

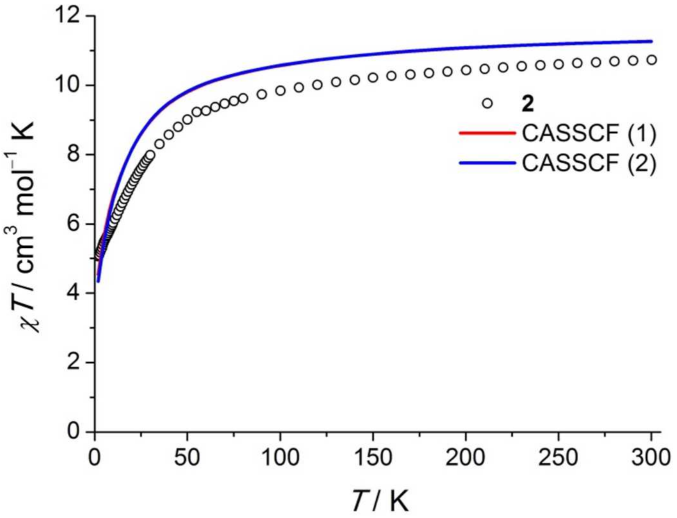

Fig. S33. Experimental and calculated χT curve for a polycrystalline sample of **2** using the CASSCF derived parameters. CASSCF (1) and (2) refer to the calculations for an isolated molecule and taking into account additional point charges, respectively.

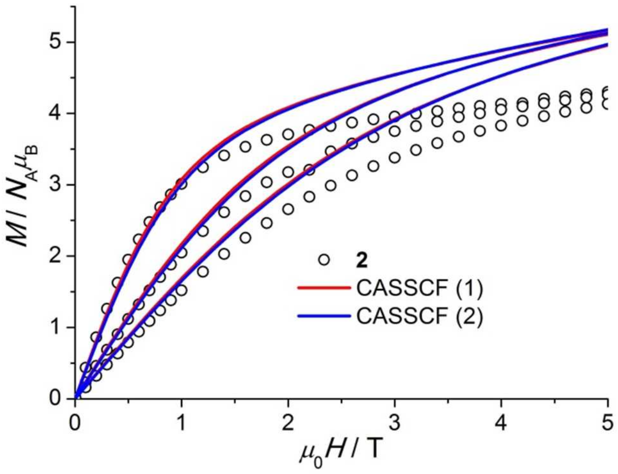

Fig. S34. Experimental and calculated magnetization curves at 2, 4 and 6 K for a polycrystalline sample of **2** using the CASSCF derived parameters. CASSCF (1) and (2) refer to the calculations for an isolated molecule and taking into account additional point charges, respectively.

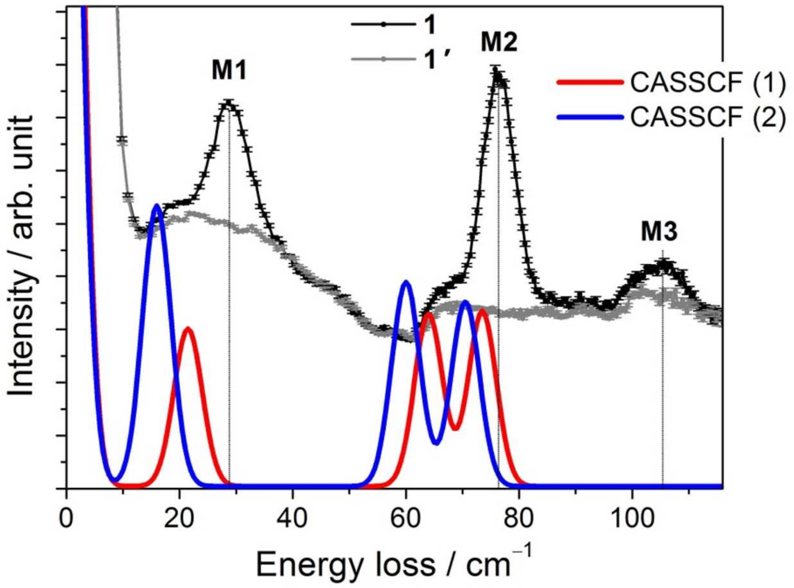

Fig. S35. Experimental and calculated INS spectrum of **3** using the CASSCF derived parameters. CASSCF (1) and (2) refer to the calculations for an isolated molecule and taking into account additional point charges, respectively.

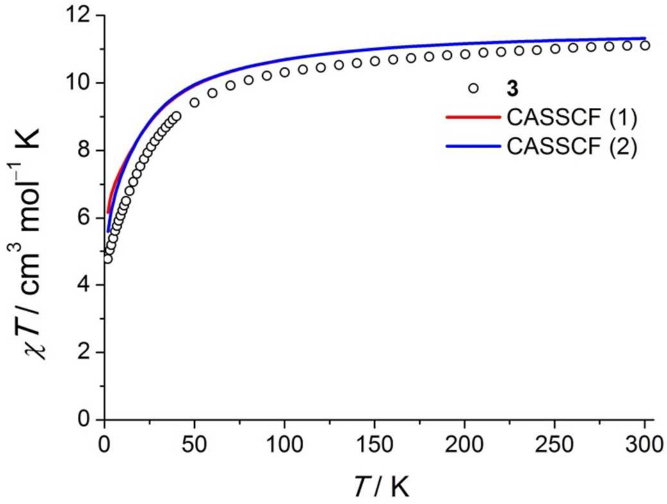

Fig. S36. Experimental and calculated χT curve for a polycrystalline sample of **3** using the CASSCF derived parameters. CASSCF (1) and (2) refer to the calculations for an isolated molecule and taking into account additional point charges, respectively.

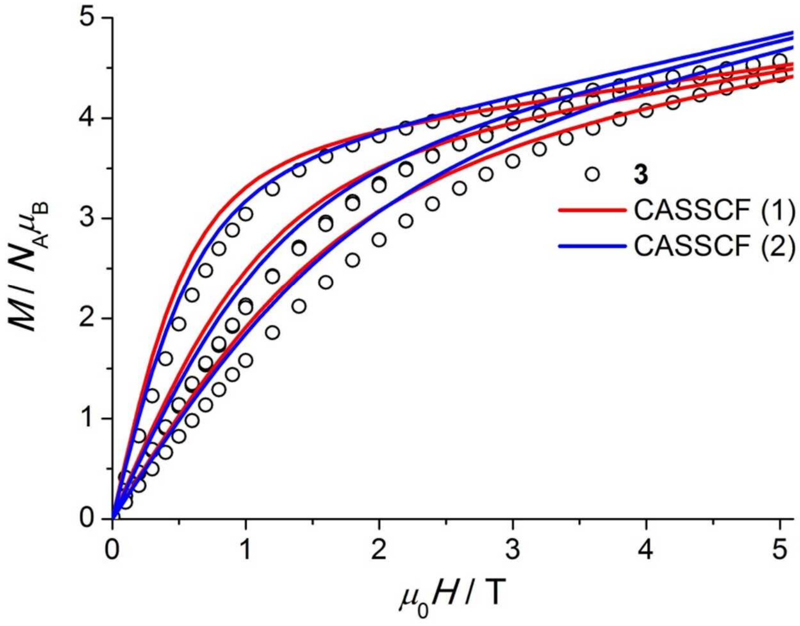

Fig. S37. Experimental and calculated magnetization curves at 2, 4 and 6 K for a polycrystalline sample of **3** using the CASSCF derived parameters. CASSCF (1) and (2) refer to the calculations for an isolated molecule and taking into account additional point charges, respectively.

6 Energy level diagrams

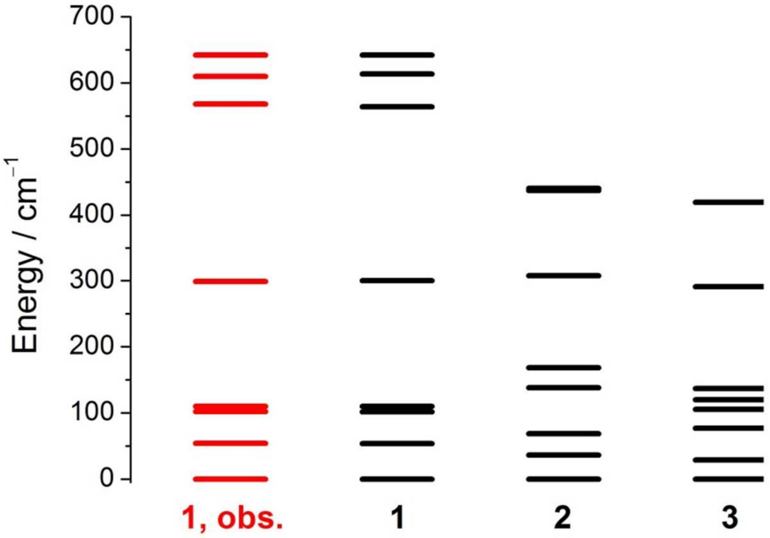

Fig. 38. Calculated energy levels for **1**–**3** using the best-fit parameters mentioned in the text. The red trace corresponds to the transitions observed by Flanagan *et al.* (ref. 11*a* of the main text) by optical spectroscopy.

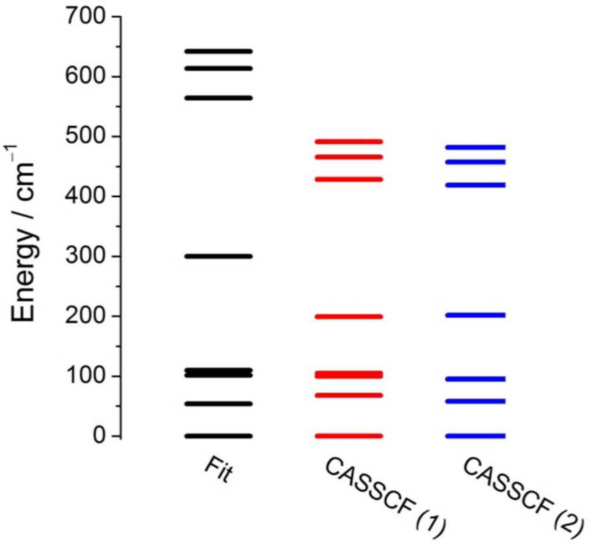

Fig. 39. Calculated energy levels for **1** using the best-fit parameters mentioned in the text and as obtained from CASSCF calculations. CASSCF (1) and (2) refer to the calculations for an isolated molecule and taking into account additional point charges, respectively.

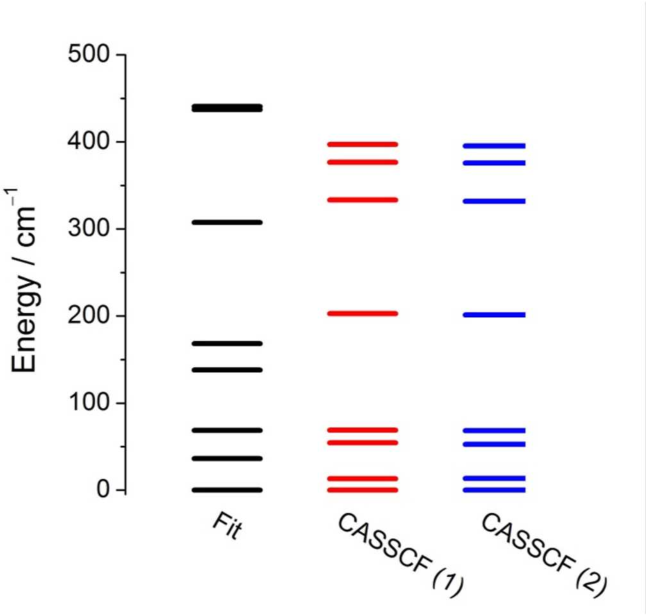

Fig. 40. Calculated energy levels for **2** using the best-fit parameters mentioned in the text. CASSCF (1) and (2) refer to the calculations for an isolated molecule and taking into account additional point charges, respectively.

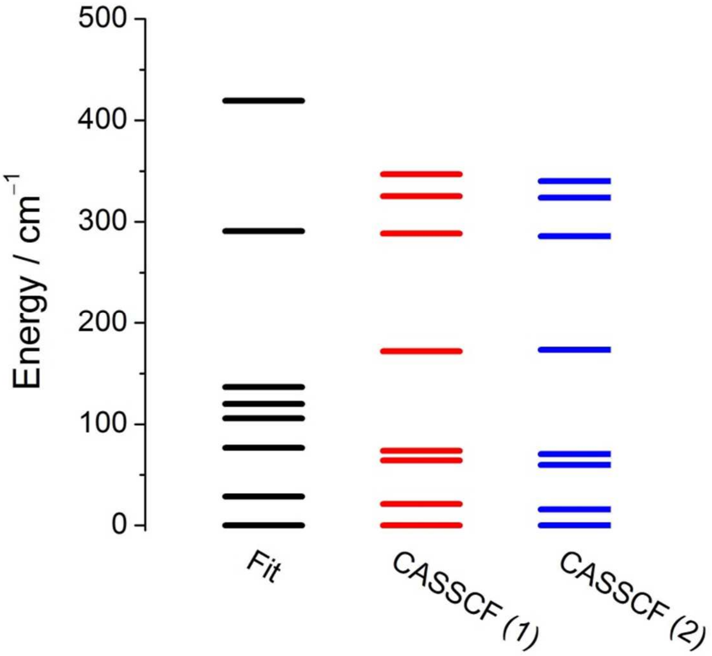

Fig. 41. Calculated energy levels for **3** using the best-fit parameters mentioned in the text. CASSCF (1) and (2) refer to the calculations for an isolated molecule and taking into account additional point charges, respectively.

7 Ac susceptibility

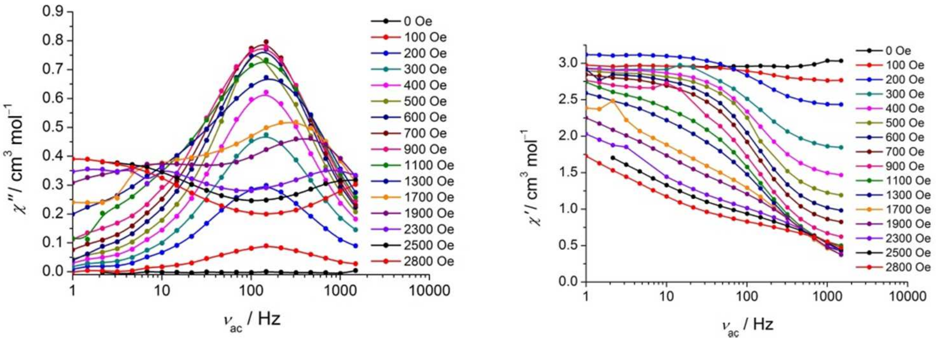

Fig. S42. Field dependence of the ac susceptibility for **1** obtained at T = 1.9 K.

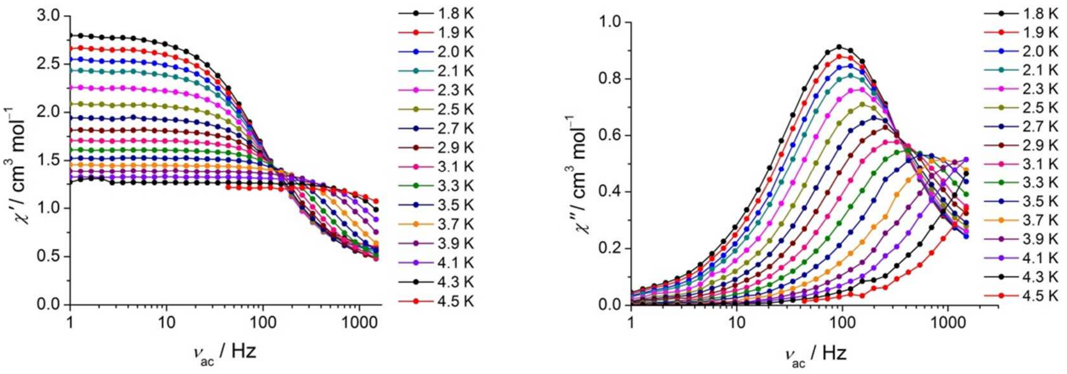

Fig. S43. Temperature dependence of the ac susceptibility for **1** obtained at H_{dc} = 900 Oe.

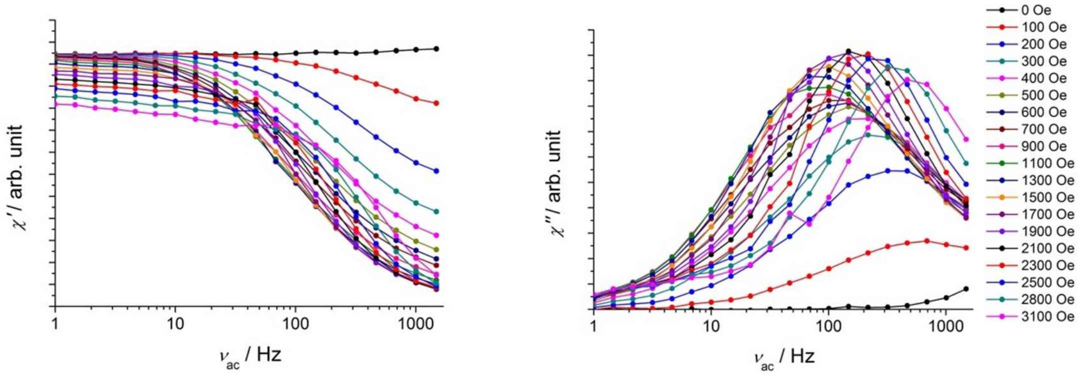

Fig. S44. Field dependence of the ac susceptibility for Er:**1′** (*ca.* 10 % doping concentration) obtained at T = 1.9 K.

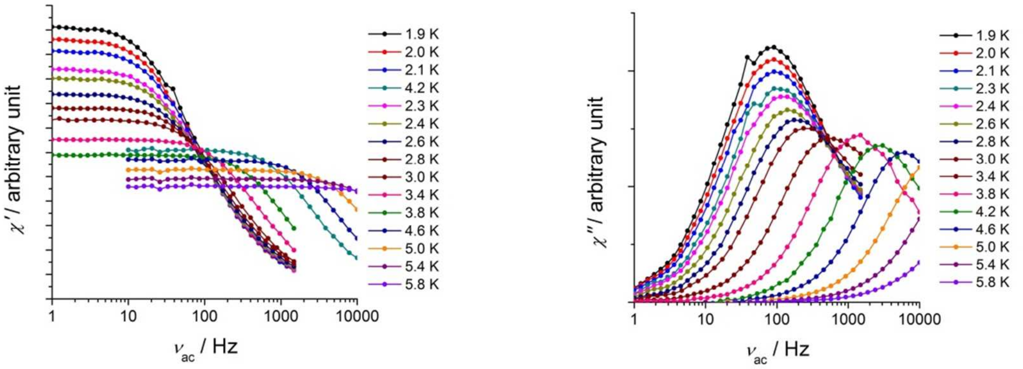

Fig. S45. Temperature dependence of the ac susceptibility for Er:**1′** (*ca.* 10 % doping concentration) obtained at H_{dc} = 1100 Oe.

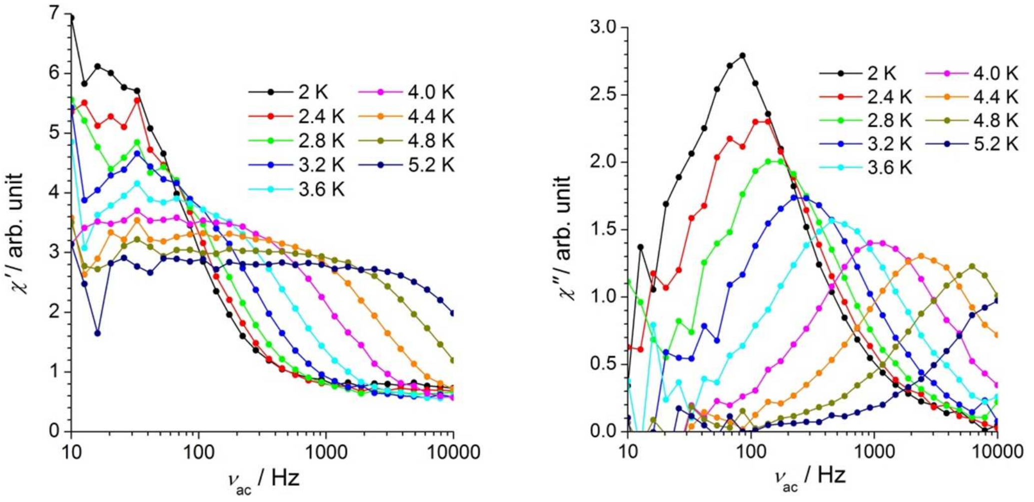

Fig. S46. Ac susceptibility of a single-crystal of **1** measured along the C_3 axis in a static field of H_{dc} = 900 Oe.

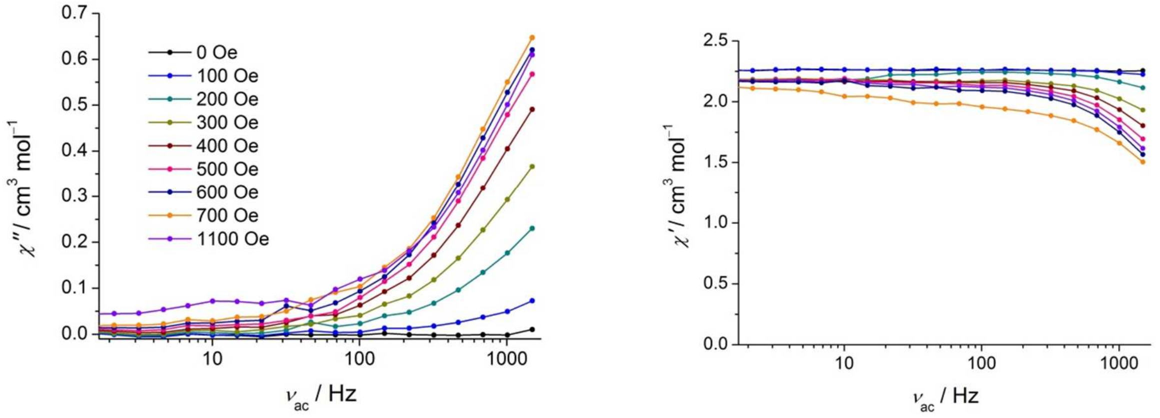

Fig. S47. Field dependence of the ac susceptibility for **2** obtained at *T* = 1.9 K.

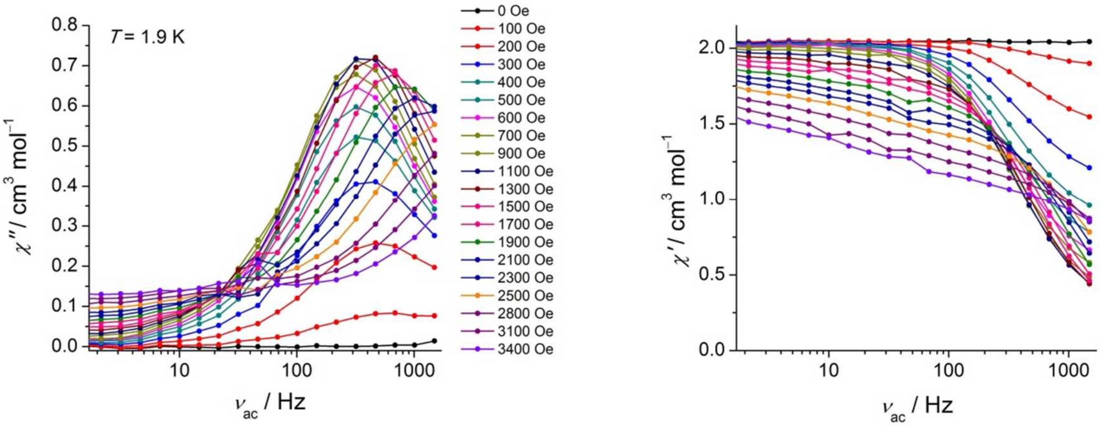

Fig. S48. Field dependence of the ac susceptibility for **3** obtained at $T = 1.9$ K.

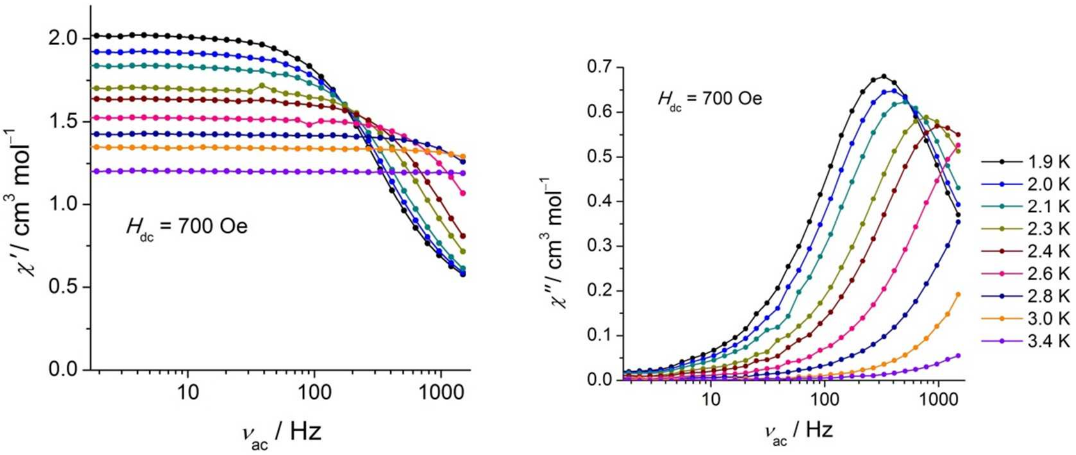

Fig. S49. Temperature dependence of the ac susceptibility for **3** obtained at $H_{dc} = 700$ Oe.

8 Relaxation times, complete fits

The field dependence of the relaxation times of **1** and of Er-doped **1′** is shown in Fig. S50(a). The tunnelling rate was modelled by a simple two-level system approach with external magnetic field H_{ext} along the z-axis, and transverse internal field B_{int} due to hyperfine interaction and dipolar fields, yielding

$$\Gamma_{\mathrm{QTM}} = \frac{1}{2}\frac{\Gamma_0}{1+\alpha^2+\alpha\sqrt{\alpha^2+1}}, \quad \text{with} \quad \alpha = \mu_0\frac{H_{\mathrm{ext}}}{2B_{\mathrm{int}}} \qquad \text{(Eq. S1)}$$

in the approximation of $\mu_0 H_{\mathrm{ext}} >> B_{\mathrm{int}}$, this reduces to the expression $\Gamma_{\mathrm{QTM}} = B_1 / (1+B_2H^2)$ used e.g. by Zadrozny *et al.* in Ref. 30*d* of the main text. The green model curve shown in Fig. S50(a) has been obtained employing B_{int} = 10 mT and Γ_0 = 95.4 µs. The blue line is obtained from $\Gamma_{\mathrm{direct}} = \beta H^{-4}$, with β = 0.27 ns Oe^4.

The temperature and field dependencies of the relaxation times of Er-doped **1′** are plotted in Fig. S50(b-e), along with fits using the complete model

$$\tau^{-1}(T,H) = CT^n + ATH^4 + \frac{B_1}{1+B_2H^2} + \frac{exp\left(-\frac{\Delta}{k_BT}\right)}{\tau_0} \qquad \text{(Eq. S2)}$$

taking into account (in the order of appearance) two-phonon Raman processes, the direct process, quantum tunneling of magnetisation and the Orbach process. The same equation was already used in Ref. 30*d* of the main text, except for the field dependence of the direct process which is different for Kramers ions (this work) and non-Kramers ions (Ref. 30*d*), respectively.

The best-fit parameters are

Including the Orbach process [Fig. S50(b,c)]	Without Orbach process [Fig. S50(d,e)]
$C = 13(5)$ s^{-1}K^{-n}	$C = 0.4(2)$ s^{-1}K^{-n}
$n = 4.5(4)$	$n = 7.5(5)$
$A = 1.9(2) \times 10^{-11}$ s^{-1}K^{-1}Oe^{-4}	$A = 2.3(2) \times 10^{-11}$ s^{-1}K^{-1}Oe^{-4}
$B_1 = 3.9(7) \times 10^3$ s^{-1}	$B_1 = 3.2(4) \times 10^3$ s^{-1}
$B_2 = 1.7(5) \times 10^{-5}$ Oe^{-2}	$B_2 = 6(1) \times 10^{-6}$ Oe^{-2}
$\Delta = 54.0$ cm^{-1} (fixed)	
τ_0=1.3(4) $\times 10^{-13}$s .	

For obvious reasons, the effective barrier Δ of the Orbach process was fixed to 54 cm^{-1} but the prefactor τ_0 was left freely varying. Interestingly, when the complete fit without including the Orbach process [cf. Fig. S50(d,e)] is performed, the temperature dependence is better reproduced while the agreement with the field dependence is slightly worse. This behavior can be attributed to being close to overparameterisation when the Orbach process is added which has to be considered when interpreting the best-fit parameters, especially the value of the exponent which in the fit without the Orbach process takes the value of n = 7.5(5) consistent with the results from the simplest approach given by Eq. (2) of the main text. Disregarding the exact value of the exponent, it is impossible to obtain an acceptable fit result without taking into account the CT^n term in the complete fits (Eq. S2), corroborating the importance of two-phonon processes at temperatures of about 4 K.

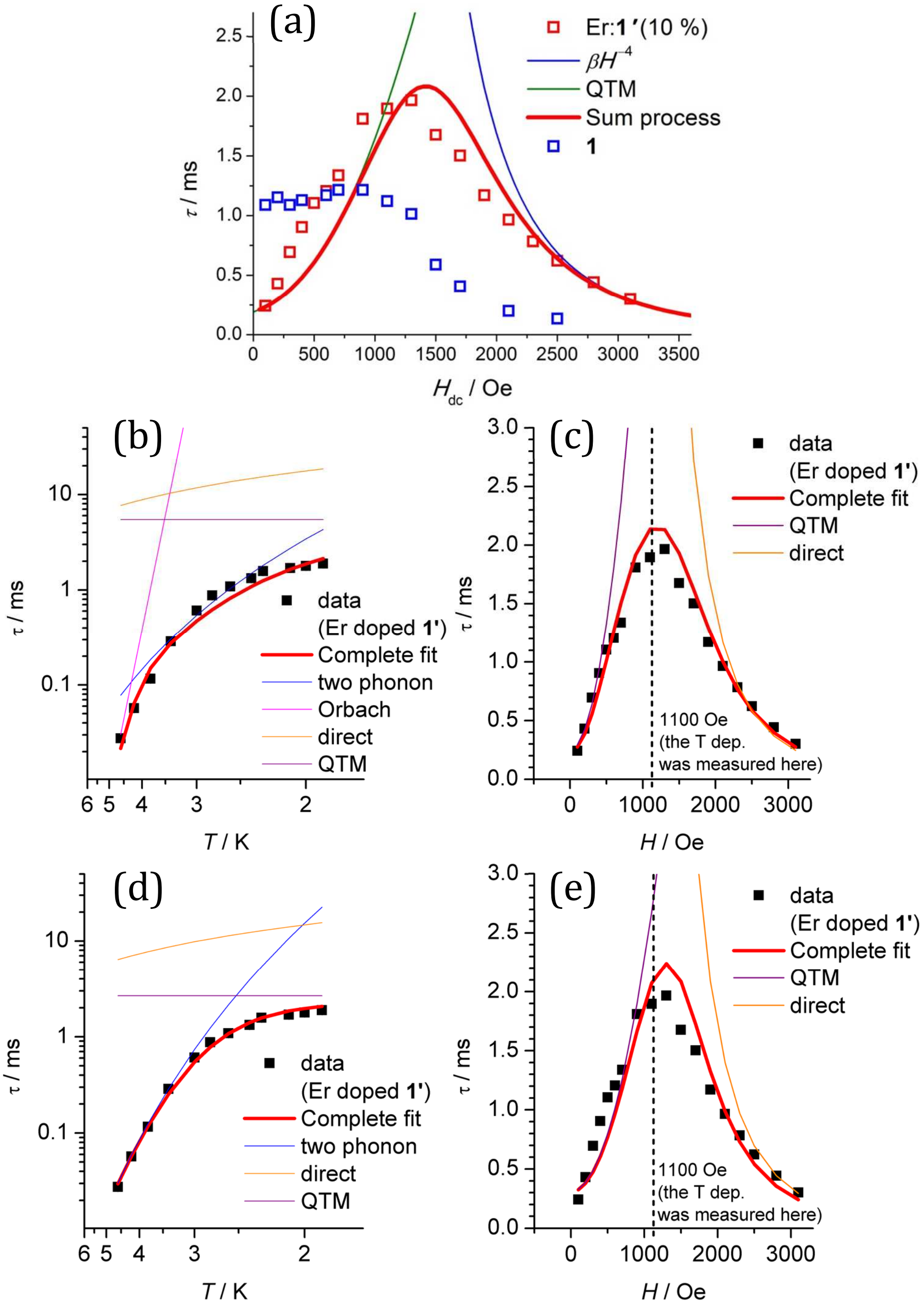

Fig. S50. (a) Field dependence of the magnetisation relaxation times of **1** and of Er:**1′** (*ca.* 10 % doping concentration) extracted from Fig. S42 and S44. Solid lines denote calculations explained in the text before. (b,c) Fits of the magnetisation relaxation times of Er:**1′** (*ca.* 10 % doping concentration) including two-phonon, direct, QTM and Orbach processes. No satisfactory reproduction is possible without inclusion of two-phonon Raman processes, neither for the temperature variation alone nor for the *T*, *H* dependence. Below ca. 4 K two-phonon Raman processes become dominant. (d,e) same as in (b,c) but without taking into account the Orbach process.

9 Hall magnetometry

The isothermal magnetization curve of a single crystal of **1** of a mass of 0.26 mg was measured with a micro-Hall magnetometer at temperatures between 1.4 and 8.4 K. The sweeping rate of the external magnetic field was varied in the range from 150 to 2300 mT/s. The crystal was aligned with respect to the magnetic field such that a maximal magnetic signal was measured. The accuracy of the alignment was estimated to be better than 5°. Fig. S51 (left) presents the raw data of hysteresis measurements for a sweeping rate of 150 mT/s at various temperatures. As commonly observed for this measurement technique, a linear slope is superimposed on the data due to a small misalignment of the sensor plane with respect to the external magnetic field of about 0.25°. This slope was corrected by assuming that the magnetization of **1** saturates at the highest applied magnetic fields. In the present case this assumption is not fully justified, since the SQUID data (Fig. 4 of the main text) evidence a small increase of *M*(*H*) even at high fields. It is emphasized that the correction procedure does not affect conclusions as regards a hysteretic behavior. The slope-corrected data are presented in Fig. S51 (right). Fig. S52 presents the slope-corrected hysteresis measurements of **1** recorded at 1.4 K for sweeping rates of the magnetic field between 150 and 2300 mT s^{-1}. Even for the highest sweeping rate of the magnetic field no opening of a hysteresis was observed.

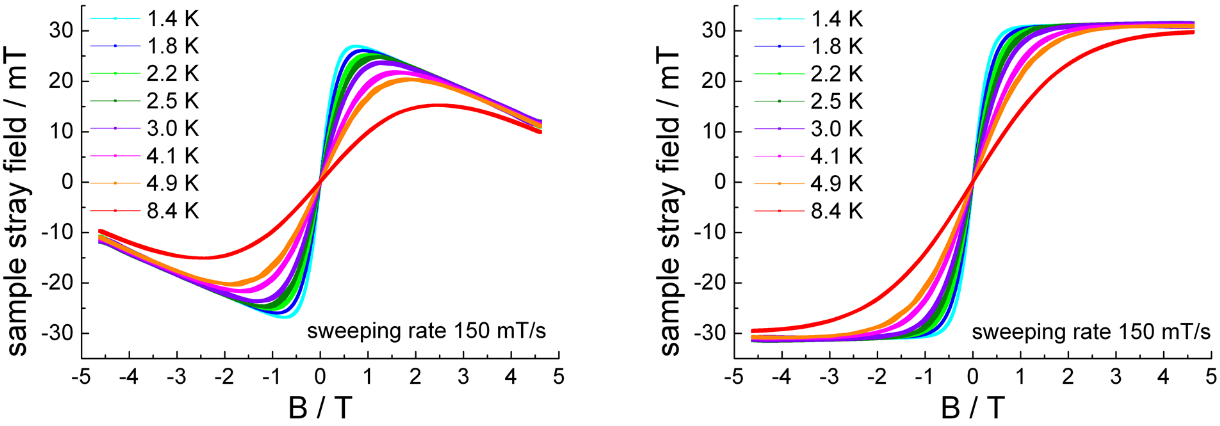

Fig. S51. Temperature dependent hysteresis measurement of **1** for a sweeping rate of the magnetic field of 150 mT/s. Left: Raw data as discussed in the text. Right: Data corrected for the slope due to a misalignment of the sensor plane with respect to the magnetic field of 0.25°.

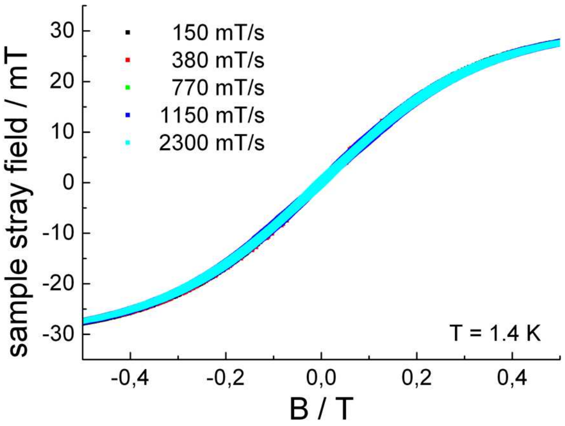

Fig. S52. Sweeping rate dependence of the hysteresis measurement of **1**.